

Letters

Passivity-Based Design of Resonant Current Controllers Without Involving Partial Derivative

Chao Gao , Shan He , *Member, IEEE*, Pooya Davari , *Senior Member, IEEE*, Ka Nang Leung , *Senior Member, IEEE*, Poh Chiang Loh , and Frede Blaabjerg , *Fellow, IEEE*

Abstract—In terms of digital control delay, dissipation of the current controller is necessary to enhance the interactive stability between grid-following converters and the grid. The key principle is to make the real part of the converter output admittance non-negative below Nyquist frequency. Besides the fundamental current control, a phase-lead compensation should be introduced for the dissipative design of harmonic resonant controllers. However, derivation of the compensation angle requires calculating the partial derivative of real part of converter output admittance, which is nontrivial, especially in the presence of grid voltage feedforward. This letter provides a simple calculation method for the compensation angle to achieve dissipativity, and its effectiveness is verified through experiments.

Index Terms—Compensation angle, current control, dissipativity, grid-following converter, resonant controller.

I. INTRODUCTION

AS VOLTAGE source converter (VSC)-based resources continue proliferating, the power grid is undergoing a transformative shift toward a power-electronic-based structure [1], [2]. In order to tackle the converter-grid interactive instability, passivity-based controller design has received significant attention [3]. The core idea is to make the real part of the converter output admittance non-negative below the Nyquist frequency using digital control (or called dissipation), and the VSC system can be stabilized regardless of wide-varied passive grid admittance [4].

In light of the current control of grid-following VSCs, the nondissipative region is mainly related to the total time delay (usually 1.5 times of sampling period) in the computation and

pulsewidth modulation (PWM) process [5], [6]. Several efforts have been made to remove the nondissipative region, such as capacitor current active damping (CCAD) [7], [8], capacitor voltage feedforward (CVFF) and CCAD [9], [10], [11], [12], and only CVFF [13]. But only a few works focus on the effect of harmonic resonant (R) controllers on dissipativity [9], [14], [15]. Specifically, R controllers can introduce an extra nondissipative region in the vicinity of harmonic frequencies even though the VSC system is dissipative without R controllers [9]. Common solution is to introduce a specific phase-lead compensation for R controllers. It is verified that neither no compensation nor compensation of computation and PWM delay can guarantee dissipativity [14], [15]. In [14], a partial-derivative-based method is proposed to solve the compensation angle, where the main challenge is the complicated derivation of compensation angle through calculating the partial derivative of real part of VSC output admittance [15]. Further, the compensation angle is strongly related to damping methods, which makes the derivation more difficult especially when using CVFF [14]. However, CVFF is often indispensable for the resonance damping and startup of grid-following VSC [10], [11].

To solve this problem, this letter proposes a simple compensation angle calculation method without involving partial derivatives. The rest of the letter is organized as follows. In Section II, a detailed system model is derived for a grid-following VSC with CCAD and CVFF. The proposed compensation angle calculation method is proposed in Section III. In the last, experimental results are presented in Section IV. Finally, Section V concludes this letter.

II. SYSTEM MODELING WITH CONVERTER-SIDE CURRENT CONTROL

With switches in Fig. 1(a) and (b) switching to converter-side current, $i_o(s)$, Fig. 1 presents the schematic circuit diagram and the detailed control block diagram of the grid-connected VSC with converter-side current control. The converter is connected to the grid through an LCL filter, with L_1 , L_2 , and C denoting the converter-side inductance, the grid-side inductance, and the filter capacitance, respectively. L_g and C_g denote the grid inductance and capacitance, respectively. The capacitor voltage ($v_c(s)$) is fed forward to a phase-locked loop (PLL) for synchronizing the

Manuscript received 11 July 2023; revised 17 August 2023; accepted 3 September 2023. Date of publication 8 September 2023; date of current version 23 October 2023. This work was supported by the Reliable Power Electronics-Based Power System project at the Department of Energy, Aalborg University, as a part of the Villum Investigator Program funded by the Villum Foundation. (Corresponding author: Shan He.)

Chao Gao, Ka Nang Leung, and Poh Chiang Loh are with the Department of Electronic Engineering, The Chinese University of Hong Kong, Hong Kong, China (e-mail: chaogao@link.cuhk.edu.hk; knleung@ee.cuhk.edu.hk; pcloh@ee.cuhk.edu.hk).

Shan He, Pooya Davari, and Frede Blaabjerg are with the Department of Energy, Aalborg University, 9220 Aalborg, Denmark (e-mail: she@energy.aau.dk; pda@energy.aau.dk; fbl@energy.aau.dk).

Color versions of one or more figures in this article are available at <https://doi.org/10.1109/TPEL.2023.3313178>.

Digital Object Identifier 10.1109/TPEL.2023.3313178

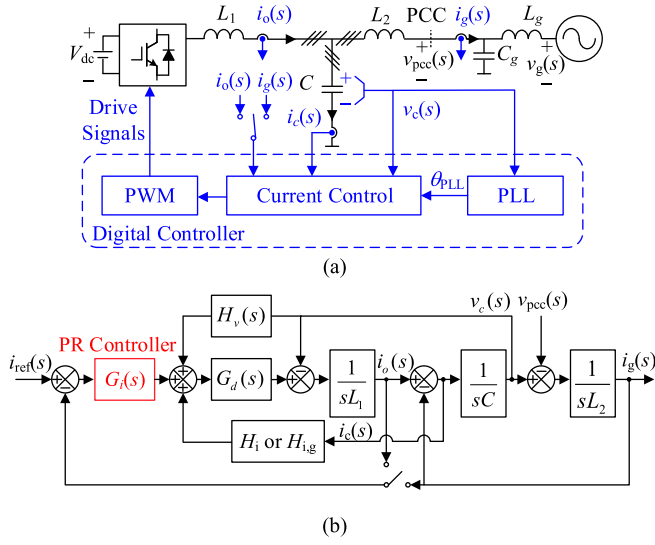


Fig. 1. General structure of a three-phase grid-connected VSC with either converter-side or grid-side current control. (a) Schematic circuit diagram. (b) Detailed control block diagram.

current reference ($i_{\text{ref}}(s)$) with the voltage at point of common coupling (PCC), $v_{\text{pcc}}(s)$, and to current control for CVFF. The capacitor current ($i_c(s)$) is fed to the current control for CCAD. The converter-side current ($i_o(s)$) is fed back for tracking $i_{\text{ref}}(s)$. Since this letter only focuses on the dissipative region around harmonic resonant frequencies of R controller, PLL is designed to have a low bandwidth to avoid affecting the frequency characteristics around harmonic frequencies [16]. Thus, its effect is ignored in the following analysis.

H_i denotes the CCAD coefficient with converter-side current control. The transfer function of CVFF is $H_v(s)$. The current controller, $G_i(s)$, is a proportional-resonant controller expressed as

$$G_i(s) = K_p + \sum_h \underbrace{K_{rh} \frac{s \cos \varphi_h - h\omega_1 \sin \varphi_h}{s^2 + h^2\omega_1^2}}_{R_h(s)} \quad (1)$$

where ω_1 is the fundamental angle frequency, h is the order of the harmonics of concern, K_p is the proportional gain, K_{rh} is the resonant gain of the R controller tuned at $h\omega_1$ ($R_h(s)$), and φ_h is the compensation angle at the resonant frequency, $h\omega_1$. The delay from the voltage reference to the output voltage is modeled as

$$G_d(s) = e^{-sT_d} \quad (2)$$

where $T_d = 1.5T_s$ is the total delay caused by computation and PWM with T_s being the sampling period. With C and L_2 regarded as a part of grid impedance, Z_g , the admittance model of the VSC with L_1 filter is derived as

$$i_o(s) = G_{\text{cl}}(s)i_{\text{ref}}(s) - Y_o(s)v_c(s) \quad (3)$$

where the closed-loop transfer function, $G_{\text{cl}}(s)$, and the output admittance, $Y_o(s)$, are, respectively, given by

$$G_{\text{cl}}(s) = \frac{G_i(s)G_d(s)}{sL_1 + G_i(s)G_d(s)} \quad (4)$$

$$Y_o(s) = \frac{1 - sH_iCG_d(s) - H_v(s)G_d(s)}{sL_1 + G_i(s)G_d(s)}. \quad (5)$$

According to the passivity theory, two conditions guarantee the system's stability: 1) $G_{\text{cl}}(s)$ is stable; and 2) $Z_g(s)$ and $Y_o(s)$ are both dissipative below the Nyquist frequency.

The first condition can be fulfilled by a properly designed K_p . It is recommended that the bandwidth of the open loop transfer function, α_c , should be smaller than a tenth of sampling angle frequency, $\omega_s/10$, and herein $\alpha_c = \omega_s/10$ is adopted. Then, K_p is given by $K_p = \alpha_c L_1$ [9], which ensures the first condition.

Provided that $Z_g(s)$ is composed of passive components, $Z_g(s)$ is passive. The dissipativity of $Y_o(s)$ relies on proper control parameters, whose design will be detailed below.

Since R controllers only affect the admittance around the resonant frequencies, they can be neglected when designing other parameters. Consequently, the real part of $Y_o(s)$ is calculated as

$$\text{Re}\{Y_o(j\omega)\} = A_1(\omega) + A_2(\omega) \quad (6)$$

where $A_1(\omega)$ is the real part of $Y_o(s)$ without CVFF, and $A_2(\omega)$ is the real part of $Y_o(s)$ introduced by CVFF, which are, respectively, expressed as

$$A_1(\omega) = \frac{(K_p - H_i L_1 C \omega^2) \cos(\omega T_d)}{(K_p \cos(\omega T_d))^2 + (\omega L_1 - H_i \sin(\omega T_d))^2} \quad (7)$$

$$A_2(\omega) = \frac{-0.5K_{ff}K_p(1 + \cos(\frac{2}{3}\omega T_d))}{(K_p \cos(\omega T_d))^2 + (\omega L_1 - H_i \sin(\omega T_d))^2} + \frac{0.5K_{ff}L_1\omega(\sin(\omega T_d) + \sin(\frac{5}{3}\omega T_d))}{(K_p \cos(\omega T_d))^2 + (\omega L_1 - H_i \sin(\omega T_d))^2}. \quad (8)$$

H_i is designed such that $A_1(\omega) \geq 0$ for $0 < \omega < \omega_s/2$. Thus, $(K_p - H_i L_1 C \omega^2)$ should change its sign at the critical frequency, $\omega_s/6$, where $\cos(\omega T_d)$ changes its sign, which gives

$$H_i = \frac{4K_p T_d^2}{\pi^2 L_1 C}. \quad (9)$$

According to [12], CVFF using moving average filter is in favor of dissipativity of $Y_o(s)$, and is herein adopted. Thus, $H_v(s)$ is given by

$$H_v(s) = K_{ff}(0.5 + 0.5e^{-sT_s}) \quad (10)$$

where K_{ff} is the CVFF coefficient, which should be designed smaller than one to ensure the low-frequency dissipativity, and is set to 0.9 in this letter.

For now, $Y_o(s)$ has been designed to be dissipative without R controllers. In the next section, the dissipative design of $Y_o(s)$ with R controller will be discussed.

III. PASSIVITY-BASED DESIGN OF RESONANT CONTROLLER WITH CONVERTER-SIDE CURRENT CONTROL

A. Conventional Compensation Angle Calculation Methods

The compensation angle, φ_h , of R controller significantly influences the dissipativity characteristics of the output admittance around resonant frequency of the R controller [14]. A direct way to calculate the compensation angle, φ_h , is to compensate for

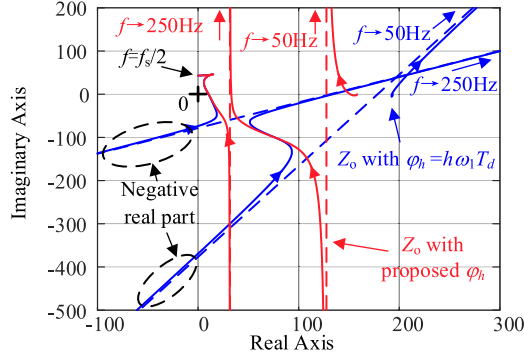


Fig. 2. Nyquist plot of output impedances with $\varphi_h = h\omega_1 T_d$, and with the proposed φ_h .

TABLE I
MAIN PARAMETERS OF A THREE-PHASE GRID-CONNECTED VSC

System Parameters		
S_n	Rated power	7 kVA
V_g	Grid phase voltage (RMS)	220 V
V_{dc}	DC-link voltage	700 V
L_1	Converter-side inductance	4 mH
L_2	Grid-side inductance	2 mH
C	Filter capacitance	10 μ F
L_g	Grid inductance	0.5 mH
C_g	Grid capacitance	30 μ F
f_{sw}	Switching frequency	4 kHz
Double-Sampling Mode Parameters		
f_s	Sampling frequency	8 kHz
K_p	Proportional current controller gain	20 Ω
K_{rh} for all h	Resonant current controller gain	4000 Ω/s
Single-Sampling Mode Parameters		
f_s	Sampling frequency	4 kHz
K_p	Proportional current controller gain	10 Ω
K_{rh} for all h	Resonant current controller gain	1000 Ω/s

the phase delay of $G_d(s)$ [9], i.e.,

$$\varphi_h = h\omega_1 T_d. \quad (11)$$

However, such a compensation angle cannot ensure dissipativity when CCAD or CVFF exists. To demonstrate this, the Nyquist plot of the corresponding output impedance, $Z_o(s) = 1/Y_o(s)$, is depicted in Fig. 2 with φ_h selected as (11), $h \in \{1, 5\}$ and other parameters listed in Table I. Note that the dissipativity of $Y_o(s)$ is equivalent to the dissipativity of $Z_o(s)$. The asymptotic lines of the Nyquist curve of $Z_o(s)$ are straight lines (dashed line in Fig. 2) as ω tends to $h\omega_1$. As long as the asymptotic line is not vertical to the real axis, the Nyquist curve is bound to pass through the left half plane, and the dissipativity is lost. This is the case of $Z_o(s)$ with (11) adopted (see the circled part in Fig. 2), proving (11) fails to ensure dissipativity.

Then, a partial-derivative-based method was proposed to solve this problem [14], which selects φ_h such that

$$\left. \frac{\partial \text{Re}\{Y_o(j\omega)\}}{\partial \omega} \right|_{\omega=h\omega_1} = 0. \quad (12)$$

Meanwhile, the second derivative should be positive

$$\left. \frac{\partial^2 \text{Re}\{Y_o(j\omega)\}}{\partial \omega^2} \right|_{\omega=h\omega_1} > 0. \quad (13)$$

The principle is that since $Y_o(jh\omega_1) = 0$, i.e., $\text{Re}\{Y_o(jh\omega_1)\} = 0$, $jh\omega_1$ should be a local minimum point of $\text{Re}\{Y_o(j\omega)\}$ otherwise $\text{Re}\{Y_o(j\omega)\}$ will be negative in the neighborhood of $h\omega_1$. Thus, (12) and (13) should be satisfied.

Even though the idea is clear, the solving process is very complex [9], [14], [15]. For that reason, another calculation method for φ_h will be proposed below, which proves to be equivalent to the partial-derivative-based method but it is much simpler.

B. Proposed Compensation Angle Calculation Method

As mentioned above, the dissipativity of $Y_o(s)$ is equivalent to the dissipativity of $Z_o(s)$. The basic principle to make $Z_o(s)$ dissipative is to design a φ_h such that the asymptotic line at the resonant frequency is vertical to the real axis. The inclination angle of the asymptotic line can be obtained by limit calculation with ω tending to $h\omega_1$. First, the left limit is

$$\begin{aligned} & \lim_{\omega \rightarrow h\omega_1^-} \angle Z_o(j\omega) \\ &= \lim_{\omega \rightarrow h\omega_1^-} \angle \frac{j\omega L_1 + G_i(j\omega)G_d(j\omega)}{1 - j\omega H_i C G_d(j\omega) - H_v(j\omega)G_d(j\omega)} \\ &= \lim_{\omega \rightarrow h\omega_1^-} \angle \left(\frac{j\omega L_1 + \left(K_p + \sum_{k \neq h} R_k(j\omega) \right) G_d(j\omega)}{1 - j\omega H_i C G_d(j\omega) - H_v(j\omega)G_d(j\omega)} \right. \\ & \quad \left. + \frac{R_h(j\omega)G_d(j\omega)}{1 - j\omega H_i C G_d(j\omega) - H_v(j\omega)G_d(j\omega)} \right). \quad (14) \end{aligned}$$

Since the magnitude of $R_h(s)$ is infinite at $h\omega_1$, any limited value added to it can be neglected. $\sum_{k \neq h} R_k(s)$ does not include a resonant frequency of $h\omega_1$, and has a finite magnitude at $h\omega_1$. Thus, the first part of (14) can be neglected. Then

$$\begin{aligned} & \lim_{\omega \rightarrow h\omega_1^-} \angle Z_o(j\omega) \\ &= \lim_{\omega \rightarrow h\omega_1^-} \angle \frac{R_h(j\omega)G_d(j\omega)}{1 - j\omega H_i C G_d(j\omega) - H_v(j\omega)G_d(j\omega)} \\ &= \lim_{\omega \rightarrow h\omega_1^-} \angle R_h(j\omega) \\ & \quad + \underbrace{\angle \frac{G_d(j\omega)}{1 - j\omega H_i C G_d(j\omega) - H_v(j\omega)G_d(j\omega)}}_{\varphi_p} \Big|_{\omega=h\omega_1} \quad (15) \end{aligned}$$

where φ_p denotes the second part of (15). For the first part of (15), the limit calculation result is

$$\lim_{\omega \rightarrow h\omega_1^-} \angle R_h(j\omega) = \frac{\pi}{2} + \varphi_h. \quad (16)$$

Substituting (16) into (15) gives

$$\lim_{\omega \rightarrow h\omega_1^-} \angle Z_o(j\omega) = \frac{\pi}{2} + \varphi_h + \varphi_p. \quad (17)$$

This is the inclination angle of the asymptotic line as ω tends to $h\omega_1^-$. In the same way, the right limit of $\angle Z_o(j\omega)$ can be obtained

$$\lim_{\omega \rightarrow h\omega_1^+} \angle Z_o(j\omega) = -\frac{\pi}{2} + \varphi_h + \varphi_p. \quad (18)$$

Thus, the phase range of $\angle Z_o(j\omega)$ at $h\omega_1$ is $[-\pi/2 + \varphi_h + \varphi_p, \pi/2 + \varphi_h + \varphi_p]$. To align the asymptotic line vertically with the real axis, featuring an inclination angle of $\pi/2$ and a phase range of $[-\pi/2, \pi/2]$ due to its positioning on the right-half plane, φ_h should be set to

$$\begin{aligned} \varphi_h &= -\varphi_p \\ &= -\angle \frac{G_d(j\omega)}{1 - j\omega H_i C G_d(j\omega) - H_v(j\omega) G_d(j\omega)} \Big|_{\omega=h\omega_1} \end{aligned} \quad (19)$$

which can be solved easily with MATLAB function *bode*. The result does not involve L_2 and L_g , because they do not affect $Y_o(s)$ or do not appear in (5). To validate the correctness of (19), the Nyquist plot of $Z_o(s)$ is depicted in Fig. 2 with φ_h selected as (19), $h \in \{1, 5\}$, and other parameters listed in Table I. The asymptotic line as ω tends to $h\omega_1$ (dashed line) is vertical to the real axis, indicating a phase range of $[-\pi/2, \pi/2]$, and therefore having no negative real part.

The proposed method is equivalent to the partial-derivative-based method. This can be verified by two special cases. First, by omitting the CVFF path, or setting $H_v(s)$ to zero, the control scheme in Fig. 1 becomes the same as that in [9]. Equation (19) is then reduced to

$$\begin{aligned} \varphi_h &= -\angle \frac{G_d(j\omega)}{1 - j\omega H_i C G_d(j\omega)} \Big|_{\omega=h\omega_1} \\ &= \angle (e^{jh\omega_1 T_d} - jh\omega_1 H_i C) \end{aligned} \quad (20)$$

which is exactly the same as the result in [9] derived by the partial-derivative-based method. Second, by omitting the CCAD path, or simply setting H_i to zero, (20) reduces to $\varphi_h = h\omega_1 T_d$, which is also exactly the same as the result in [14].

As for another parameter of the R controller, the resonant gain, K_{rh} , should be set to strike an equilibrium between fast dynamic response and good harmonic selectivity [4]. Furthermore, it is important to note that an elevated K_{rh} can potentially compromise the dissipativity when the CVFF strategy is applied [4]. Considering above factors, K_{rh} is set to 4000 for all h under a sampling frequency of 8000 Hz.

Indeed, this letter focuses on the analysis of converter-side current-controlled VSC to exemplify the proposed method. However, it is important to emphasize that this specific illustration does not preclude the applicability of the method to a

broader range of systems. As demonstrated further, the method will also be applied to grid-side current control in the upcoming section.

IV. EXTENSION TO GRID-SIDE CURRENT CONTROL

With the switches in Fig. 1(a) and (b) switching to grid-side current, $i_g(s)$, Fig. 1(a) and (b) presents the schematic circuit diagram and the detailed control block diagram of VSC with grid-side current control, respectively. The admittance model of the VSC with LCL filter can be expressed as

$$i_g(s) = G_{cl,g}(s)i_{ref}(s) - Y_{o,g}(s)v_{pcc}(s) \quad (21)$$

where $G_{cl,g}(s)$ represents the closed-loop transfer function, and $Y_{o,g}(s)$ is the output admittance whose expression (22) is shown at the bottom of this page. With a similar manner as converter-side current control, the CCAD coefficient $H_{i,g}$ for grid-side current control is derived as [11]

$$H_{i,g} = \frac{4K_p T_d^2}{\pi^2 L_1 C} - K_p. \quad (23)$$

With the proposed method elaborated in Section III-B, the compensation angle, φ_h , of $R_h(s)$ with grid-side current control can be derived as

$$\begin{aligned} \varphi_h &= \\ &= -\angle \frac{G_d(j\omega)}{1 - \omega^2 L_1 C - j\omega H_i C G_d(j\omega) - H_v(j\omega) G_d(j\omega)} \Big|_{\omega=h\omega_1} \end{aligned} \quad (24)$$

which ensures the dissipativity of $Y_{o,g}(s)$.

The fulfillment of the second condition of the passivity theory is now accomplished. To satisfy the first condition (internal stability), the stability analysis is undertaken through the transformation to converter-side current control, as expounded in [11]. According to [11], the equivalence between grid-side current control and converter-side current control is maintained, preserving the integrity of all controllers depicted in Fig. 1(b), with the sole alteration being the replacement of the CCAD coefficient with

$$H_{i,eg} = H_{i,g} + G_i(s). \quad (25)$$

As illustrated in Fig. 3, the admittance model of VSC with grid-side current control [see Fig. 3(a)] can be equivalently transformed to Fig. 3(b) comprising an admittance model of VSC with converter-side current control. Thus, by selecting the same K_p as converter-side current control, the independent current source $G_{cl}(s)i_{ref}$ is stabilized. Moreover, $Y_o(s)$ is dissipative due to the dissipativity of $Y_{o,g}(s)$. This is evident from the fact that the disparity between these two models involves only two passive components, C and L_2 , both characterized by zero resistance.

$$Y_{o,g}(s) = \frac{1 + s^2 L_1 C - s C H_{i,g} G_d(s) - H_v(s) G_d(s)}{s^3 L_1 L_2 C - s^2 L_2 C H_{i,g} G_d(s) + s(L_1 + L_2) - s L_2 H_v(s) G_d(s) + G_i(s) G_d(s)} \quad (22)$$

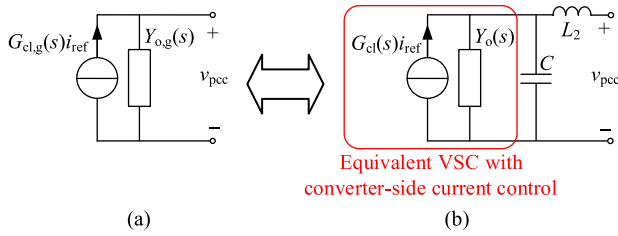


Fig. 3. Equivalence between (a) admittance model of VSC with grid-side current control and (b) admittance model of VSC with converter-side current control.

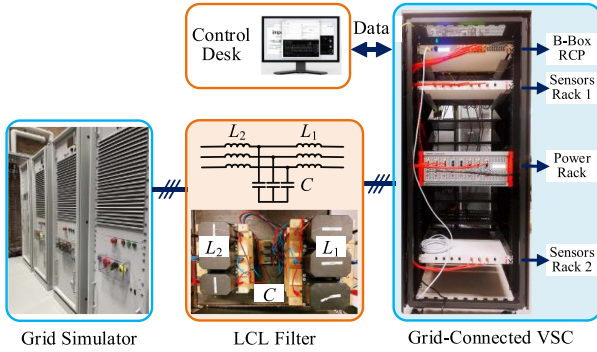


Fig. 4. Downscaled grid-connected VSC with an *LCL* filter.

Due to the equivalence, the two independent current sources in Fig. 3(a) and (b) have the following relationship:

$$G_{cl,g}(s)i_{ref} = \frac{1/[sL_2Y_o(s)]}{1 + Y_{CL_2}/Y_o(s)}G_{cl}(s)i_{ref} \quad (26)$$

where $Y_{CL_2} = sC + 1/(sL_2)$. To interpret (26) from the framework of passivity theory, the dissipativity of $Y_o(s)$ and the stability of $G_{cl}(s)$ together ensure the stability of $G_{cl,g}(s)$, i.e., the internal stability of grid-side current control.

V. EXPERIMENTAL VALIDATION

To further verify the theoretical analysis, experiments are carried out on a three-phase grid-connected VSC with an *LCL* filter, as shown in Fig. 4. The grid is emulated with a linear amplifier APS 15000. The VSC and the control platform are a PEB-SiC-8024 module and a B-BOX RCP control platform from Imperix, respectively. To verify the effectiveness of the proposed method below and beyond the current control bandwidth, α_c, h is selected to be 1, 5, 7 (below the bandwidth), 17, and 19 (beyond the bandwidth).

A. Converter-Side Current Control

In this subsection, grid impedance is assumed to contain only an inductor L_g , and double-sampling mode is adopted. Relevant parameters are presented in Table I. Fig. 5 shows the frequency responses of $Y_o(s)$, with different compensation angle selections, and the equivalent grid admittance $Y_g(s) = 1/(sL_2 + sL_g) + sC$. As it can be seen, with φ_h selected as (11), $Y_o(s)$ is not dissipative, and the phase margins (PMs) of the system are negative around 17th- and 19th-order harmonics, meaning the system is unstable.

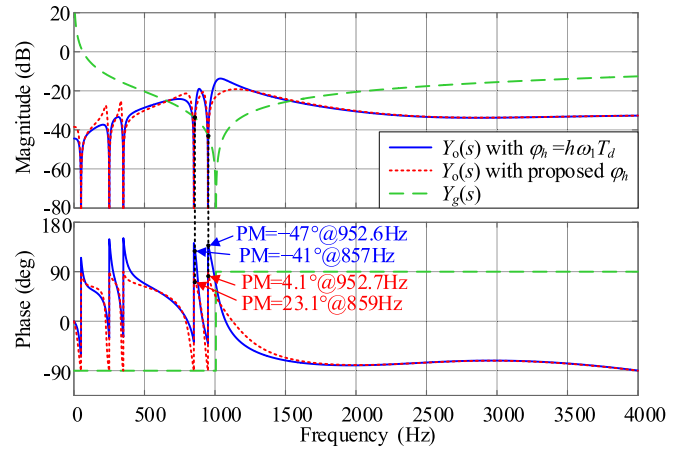


Fig. 5. Frequency responses of the equivalent grid admittance, $Y_g(s)$, and the output admittances of converter-side current-controlled VSC using the compensation angle, $\varphi_h = h\omega_1 T_d$, and the proposed φ_h .

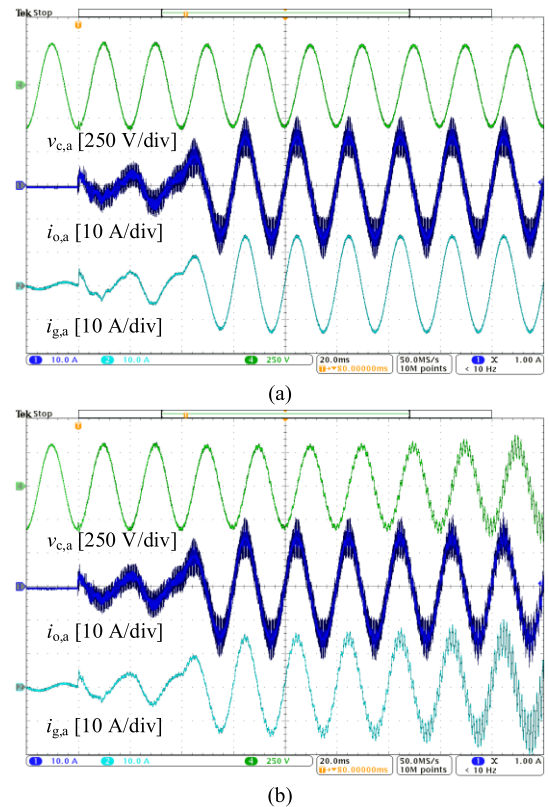


Fig. 6. Experimental waveforms of the double-sampling converter-side current-controlled VSC with compensation angle calculated by (a) proposed method, and (b) conventional method ($\varphi_h = h\omega_1 T_d$) (11).

Whereas with proposed φ_h selected, $Y_o(s)$ is dissipative, and PMs of the system are positive, i.e., the system is stable.

In the experimental setup, the dc-link connects solely to a capacitor, devoid of a dedicated dc voltage source. To manage this, a dc voltage controller is engaged to maintain the dc-link voltage. Fig. 6 shows the corresponding experimental results. After the converter is started, the q -axis current reference remains zero, and the d -axis current reference is given by dc voltage controller to establish the dc-link voltage. After 0.04 s when the dc-link

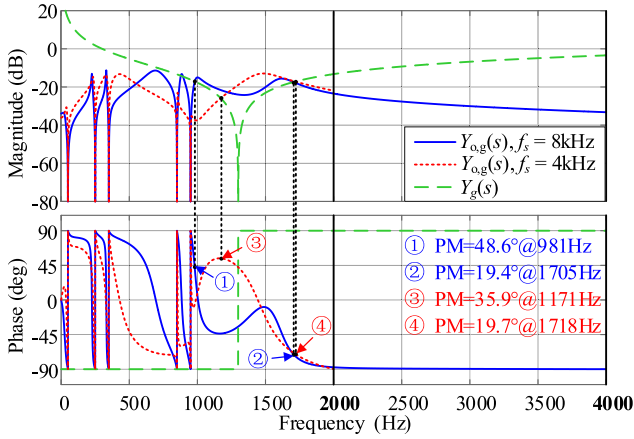


Fig. 7. Frequency responses of the equivalent grid admittance, $Y_g(s)$, and the converter output admittances of grid-side current-controlled VSC with $f_s = 8$ kHz, and with $f_s = 4$ kHz.

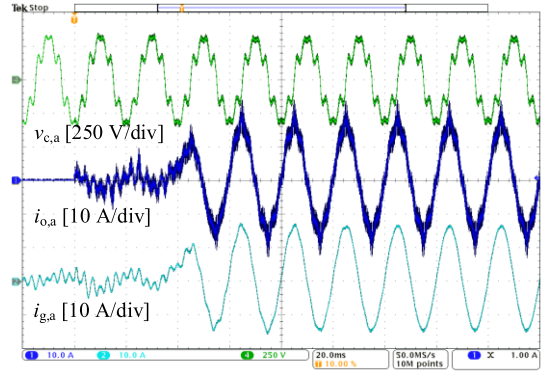
voltage is established, the q -axis reference is shifted to 15 A. As it can be seen, the system is stable with proposed φ_h [see Fig. 6(a)] since dissipativity is achieved. However, the system with $\varphi_h = h\omega_1 T_d$ is unstable [see Fig. 6(b)]. This instability leads to a gradual escalation of harmonics due to the loss of dissipativity. These findings align consistently with those presented in Fig. 5.

B. Grid-Side Current Control

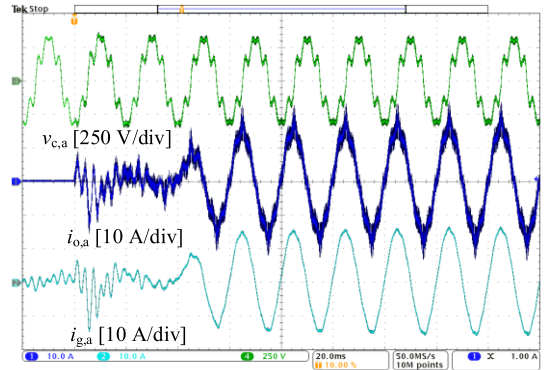
In this subsection, grid-side current control performance is assessed. Additionally, in Fig. 1(a), C_g is linked to the grid for testing under varied conditions corresponding a grid admittance: $Y_g(s) = 1/(sL_g) + sC_g$. Both double-sampling mode ($f_s = 8$ kHz) and single-sampling mode ($f_s = 4$ kHz) are implemented. Accordingly, K_p of single-sampling mode is halved to align with the principle that bandwidth relates proportionally to sampling frequency. Other parameters can be found in Table I.

Fig. 7 shows the frequency responses of the grid admittance, $Y_g(s)$, and output admittances of VSC, $Y_{o,g}(s)$, as implemented in both double-sampling and single-sampling modes. As can be seen from Fig. 7, both output admittances are dissipative beneath their respective Nyquist frequencies (4 kHz for double-sampling and 2 kHz for single-sampling). Additionally, their positive PMs signify the stability of the system in both sampling modes. Notably, it is important to exclude consideration of the output admittance beyond the Nyquist frequency range, given that the employed s -domain analysis method holds precision solely within the confines of the Nyquist frequency. Importantly, for the single-sampling mode, the 19th harmonic frequency (950 Hz) surpasses the bandwidth of 400 Hz by a substantial margin. This stark contrast conclusively demonstrates the efficacy of the proposed method in stabilizing the system, independent of the relationship between the resonant frequencies of the R controllers and the bandwidth.

Fig. 8 presents experimental waveforms illustrating the startup of the grid-side current-controlled VSC, comparing both double-sampling mode [Fig. 8(a)] and single-sampling mode [Fig. 8(b)]. The grid voltage integrates 10% fifth harmonic and 10% seventh harmonic components. Notably, the single-sampling mode's startup current is substantially higher,



(a)



(b)

Fig. 8. Experimental waveforms of grid-side current-controlled VSC with (a) double-sampling mode and (b) single-sampling mode (10% fifth harmonic and 10% seventh harmonic in grid voltage).

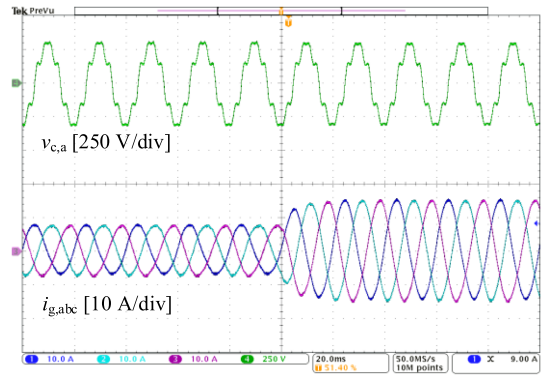


Fig. 9. Experimental waveforms of the double-sampling grid-side current-controlled VSC following a current reference shift from 7.5 to 15 A (10% fifth harmonic and 10% seventh harmonic in grid voltage).

around 14 A, in contrast to the double-sampling mode's startup current of approximately 5 A. This discrepancy can be attributed to the extended delay intrinsic to the single-sampling mode, adversely influencing overall system performance.

Fig. 9 captures the experimental waveforms of the double-sampling grid-side current-controlled VSC, following a step change in current reference from 7.5 to 15 A. The grid voltage, v_g , comprises 10% fifth harmonic and 10% seventh harmonic components. The displayed dynamics highlight the rapid response of the system using double-sampling, attaining settling within approximately 0.02 s.

VI. CONCLUSION

This letter introduces an innovative and straightforward calculation approach for determining the compensation angle in the design of passivity-based R controllers, eliminating the need for intricate partial derivative calculations. The proposed method ensures the dissipative nature of the output admittance of the VSC below the Nyquist frequency. The step-by-step procedure of this approach is meticulously elucidated, initially demonstrated within the framework of converter-side current control, and subsequently extended to encompass grid-side current control. The validity of the proposed method is substantiated through experiments.

REFERENCES

- [1] F. Blaabjerg, Y. Yang, D. Yang, and X. Wang, "Distributed power generation systems and protection," *Proc. IEEE*, vol. 105, no. 7, pp. 1311–1331, Jul. 2017.
- [2] Y. Gu and T. C. Green, "Power system stability with a high penetration of inverter-based resources," *Proc. IEEE*, vol. 111, no. 7, pp. 832–853, Jul. 2023.
- [3] L. Harnefors, X. Wang, A. G. Yepes, and F. Blaabjerg, "Passivity-based stability assessment of grid-connected VSCs—An overview," *IEEE J. Emerg. Sel. Topics Power Electron.*, vol. 4, no. 1, pp. 116–125, Mar. 2016.
- [4] L. Harnefors, L. Zhang, and M. Bongiorno, "Frequency-domain passivity based current controller design," *IET Power Electron.*, vol. 1, no. 4, pp. 455–465, Dec. 2008.
- [5] X. Wang and F. Blaabjerg, "Harmonic stability in power electronic-based power systems: Concept, modeling, and analysis," *IEEE Trans. Smart Grid*, vol. 10, no. 3, pp. 2858–2870, May 2019.
- [6] S. He, D. Zhou, X. Wang, Z. Zhao, and F. Blaabjerg, "A review of multisampling techniques in power electronics applications," *IEEE Trans. Power Electron.*, vol. 37, no. 9, pp. 10514–10533, Sep. 2022.
- [7] X. Wang, Y. He, D. Pan, H. Zhang, Y. Ma, and X. Ruan, "Passivity enhancement for LCL-filtered inverter with grid current control and capacitor current active damping," *IEEE Trans. Power Electron.*, vol. 37, no. 4, pp. 3801–3812, Apr. 2022.
- [8] S. Li and H. Lin, "Passivity enhancement-based general design of capacitor current active damping for LCL-type grid-tied inverter," *IEEE Trans. Power Electron.*, vol. 38, no. 7, pp. 8223–8236, Jul. 2023.
- [9] L. Harnefors, A. Yepes, A. Vidal, and J. Gandoy, "Passivity-based controller design of grid-connected VSCs for prevention of electrical resonance instability," *IEEE Trans. Ind. Electron.*, vol. 62, no. 2, pp. 702–710, Feb. 2015.
- [10] C. Xie, K. Li, J. Zou, and J. Guerrero, "Passivity-based stabilization of LCL-type grid-connected inverters via a general admittance model," *IEEE Trans. Power Electron.*, vol. 35, no. 6, pp. 6636–6648, Jun. 2020.
- [11] S. He, Z. Yang, D. Zhou, X. Wang, R. W. De Doncker, and F. Blaabjerg, "Dissipativity robustness enhancement for LCL-filtered grid-connected VSCs with multisampled grid-side current control," *IEEE Trans. Power Electron.*, vol. 38, no. 3, pp. 3992–4004, Mar. 2023.
- [12] S. He and F. Blaabjerg, "Design-oriented dissipativity robustness enhancement for current control of LCL-filtered grid-following VSCs," in *Proc. IEEE Appl. Power Electron. Conf. Expo.*, 2023, pp. 2796–2800.
- [13] C. Xie, J. Zou, D. Liu, and J. Guerrero, "Passivity-based design of grid-side current-controlled LCL-type grid-connected inverters," *IEEE Trans. Power Electron.*, vol. 35, no. 9, pp. 9813–9823, Sep. 2020.
- [14] L. Harnefors, A. Yepes, A. Vidal, and J. Gandoy, "Passivity-based stabilization of resonant current controllers with consideration of time delay," *IEEE Trans. Power Electron.*, vol. 29, no. 12, pp. 6260–6263, Dec. 2014.
- [15] Z. Zhou et al., "Selective harmonic voltage control for STATCOMs in wind power plants," *IEEE Trans. Power Del.*, vol. 38, no. 3, pp. 2183–2194, Jun. 2023.
- [16] Z. Yang et al., "Wideband dissipativity enhancement for grid-following VSC utilizing capacitor voltage feedforward," *IEEE J. Emerg. Sel. Topics Power Electron.*, vol. 11, no. 3, pp. 3138–3151, Jun. 2023.